



# Parity measurement in the strong dispersive regime of circuit quantum acoustodynamics

Uwe von Lüpke<sup>1,2,3</sup> , Yu Yang<sup>1,2,3</sup>, Marius Bild<sup>1,2,3</sup>, Laurent Michaud<sup>1,2</sup>, Matteo Fadel<sup>1,2</sup> and Yiwen Chu<sup>1,2</sup>

**Mechanical resonators are emerging as an important new platform for quantum science and technologies. A large number of proposals for using them to store, process and transduce quantum information motivates the development of increasingly sophisticated techniques for controlling mechanical motion in the quantum regime. By interfacing mechanical resonators with superconducting circuits, circuit quantum acoustodynamics can make a variety of important tools available for manipulating and measuring motional quantum states. Here we demonstrate the direct measurements of phonon number distribution and parity of non-classical mechanical states. We do this by operating our system in the strong dispersive regime, where a superconducting qubit can be used to spectroscopically resolve the phonon Fock states. These measurements are some of the basic building blocks for constructing acoustic quantum memories and processors. Furthermore, our results open the door for performing even more complex quantum algorithms using mechanical systems, such as quantum error correction and multimode operations.**

The quantum properties of solid-state mechanical objects have now been unequivocally demonstrated through a number of seminal experiments<sup>1–6</sup>. By interfacing mechanical objects with the strong quantum nonlinearity of superconducting qubits and drawing close analogies to the well-developed field of circuit quantum electrodynamics (cQED), circuit quantum acoustodynamics (cQAD) has become a particularly powerful paradigm for creating and studying mechanical quantum states<sup>1–4</sup>. At the same time, mechanical resonators present a set of unique and useful properties that distinguish them from their electromagnetic counterparts used in cQED. For example, acoustic resonators can be more compact, suffer less from crosstalk and exhibit longer lifetimes<sup>7,8</sup> than electromagnetic resonators. The fact that they are massive mechanical objects that exhibit quantum behaviour also makes them interesting platforms for investigating a variety of questions in fundamental physics<sup>9,10</sup>.

A clear and immediate goal for the field is then to use mechanical devices to demonstrate more complex quantum operations. To achieve this challenging goal, cQAD allows us to adapt tools and techniques from other fields. A particularly useful set of tools becomes available when a coupled qubit–resonator system reaches the strong dispersive regime, where an excitation in the qubit (resonator) results in a shift in the resonator (qubit) frequency that exceeds the decoherence rates of both systems<sup>11,12</sup>. The dispersive interaction is nowadays used ubiquitously in cQED systems for quantum non-demolition (QND) measurements of the qubit or resonator state<sup>13,14</sup>. In particular, it allows for the QND measurements of the photon number parity of a resonator without revealing the underlying photon number distribution. This is, for example, a crucial error syndrome measurement in many error correction schemes for quantum information encoded in harmonic oscillators<sup>15,16</sup>. The basic physics of cQAD is, in principle, analogous to cQED, and the strong dispersive regime has been shown with a phononic crystal<sup>3</sup> and surface acoustic wave resonators<sup>4</sup>. However, it has thus far been challenging for cQAD systems to reach a regime where

the dispersive interaction is sufficiently large compared with decoherence to allow for complex quantum operations. This is largely because it is difficult to maintain state-of-the-art coherence times for both qubits and mechanical resonators as they are combined into a single device. Nevertheless, previous works have shown that cQAD systems based on bulk acoustic wave resonators (HBAR) are promising for achieving a good balance between sufficiently long coherence times and electromechanical coupling strength<sup>17</sup>.

In this work, we experimentally demonstrate a cQAD system operating in the strong dispersive regime and use it to perform measurements of the phonon number distribution and parity of the quantum states of an HBAR. As described in previous work<sup>1</sup>, our system consists of a plano-convex HBAR fabricated using piezoelectric aluminium nitride (AlN) on a sapphire substrate and a superconducting qubit on a separate sapphire chip, which are then combined into a device called the  $\hbar$ BAR. The AlN couples the electric field of the qubit with the strain field of the HBAR modes, resulting in a Jaynes–Cummings (JC)-type interaction between the two quantum systems. Here we use a single-junction, non-flux tunable transmon qubit and house the  $\hbar$ BAR inside a superconducting Al cavity, which improves the coherence time of the qubit compared with previous devices. This improvement is crucial for reaching the strong dispersive regime. All the device parameters are shown in Supplementary Table 1. All the frequency tuning is performed by applying microwave drives to Stark shift the qubit instead of applying an external magnetic field<sup>18</sup>. The assembled  $\hbar$ BAR is shown in Fig. 1a, with the three-dimensional transmon visible through the HBAR chip. The two components are aligned and assembled using an industrial flip-chip bonder, which improves the reproducibility and robustness compared with devices used in previous work<sup>19</sup>. The magnified view (Fig. 1b) indicates good alignment between the qubit electrode and HBAR.

The HBAR supports a complex and dense mode structure. The acoustic velocities and dimensions of the resonator result in a longitudinal free spectral range (FSR) of  $\sim 12$  MHz, whereas the frequency

<sup>1</sup>Department of Physics, ETH Zürich, Zurich, Switzerland. <sup>2</sup>Quantum Center, ETH Zürich, Zurich, Switzerland. <sup>3</sup>These authors contributed equally: Uwe von Lüpke, Yu Yang, Marius Bild. ✉e-mail: [vluepke@phys.ethz.ch](mailto:vluepke@phys.ethz.ch); [yiwen.chu@phys.ethz.ch](mailto:yiwen.chu@phys.ethz.ch)

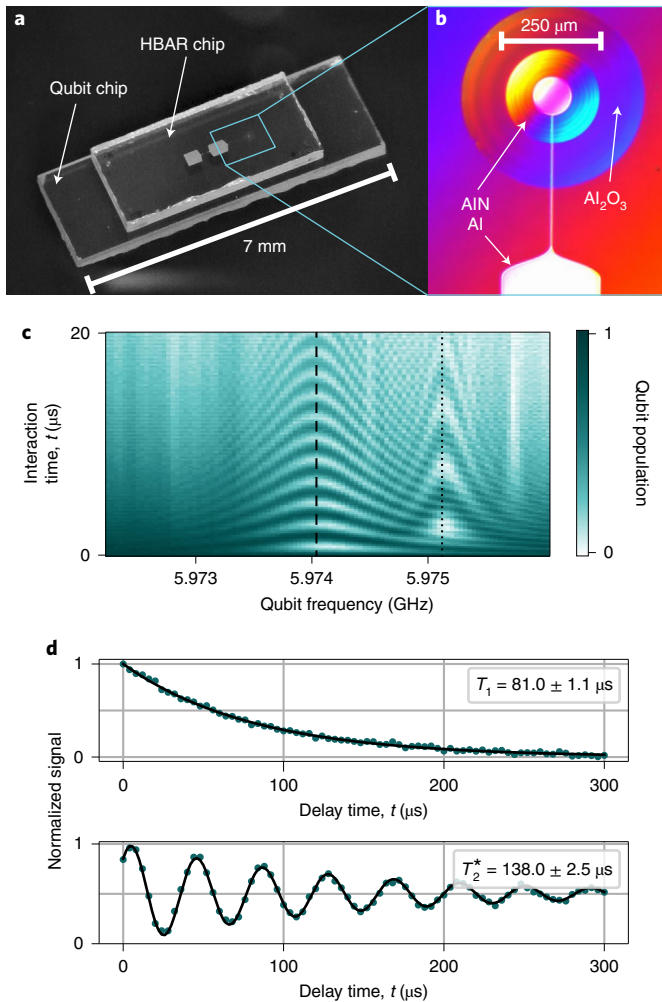


**Fig. 1 | Characterization of the hBAR device.** **a**, Photograph of the flip-chip-bonded hBAR device. **b**, Optical microscopy image of the qubit antenna and HBAR. The circles around the qubit antenna are the edges of the dome feature etched into the substrate. The Newton rings visible on the convex acoustic resonator surface are used in the alignment process. The colour is a result of the microscope light interfering between the chip surfaces. **c**, Vacuum Rabi oscillations between the qubit and phonon modes. The lines indicate the frequencies of the LG-00 (dashed) and LG-10 (dotted) modes. **d**, Energy relaxation (top) and Ramsey coherence measurement (bottom) of the LG-00 phonon mode. The green dots are data points and the black solid lines are fits to the exponential (top) and exponential sine (bottom) functions. The phase at the first point of the  $T_2^*$  measurement is a result of the qubit-phonon detuning during the delay time combined with the finite duration of the SWAP operation.

spacing between the modes with different Laguerre–Gaussian (LG) transverse-mode numbers is  $\sim 1$  MHz. This puts constraints on the range of device parameters that would allow us to use the qubit for dispersive measurements of a single acoustic mode. First, we would like the coupling strength  $g$  of the qubit to the LG-00 mode to be larger than to those with higher-order transverse-mode numbers. Second,  $g$  and detuning  $\Delta = \omega_q - \omega_m$  between the qubit frequency  $\omega_q$  and phonon frequency  $\omega_m$  should be much smaller than the FSR. If these constraints are satisfied, the effective Hamiltonian of our system in the dispersive regime of  $\Delta \gg g$  can be approximated as<sup>20</sup>

$$H/\hbar \approx \omega_m a^\dagger a + \frac{1}{2} (\omega_q + \chi a^\dagger a) \sigma_z. \quad (1)$$

Here  $a$  is the lowering operator for the acoustic mode,  $\sigma_z$  is the Pauli  $z$  operator for the qubit and  $\frac{1}{2} \chi a^\dagger a \sigma_z$  is the dispersive interaction term that shifts the qubit frequency by  $\chi a^\dagger a$ , where<sup>21</sup>

$$\chi = -2 \frac{|g|^2}{\Delta} \frac{\alpha}{\Delta - \alpha} \approx 2 \frac{|g|^2}{\Delta} \quad (2)$$

is the qubit frequency shift per phonon. The approximation is valid in our case, where  $\Delta$  is much smaller than  $\alpha$ —the anharmonicity of the qubit. We note that this is the opposite limit from the usual case in cQED, where typically  $\Delta \gg \alpha$ . Furthermore, to satisfy the requirement of  $g \ll \text{FSR}$ ,  $g$  in our system is limited to  $\lesssim 1$  MHz, which is at least one order of magnitude smaller than most cQED systems. Despite these constraints, we now show that the design and fabrication of our system leads to coherence times that are sufficient for operation in the strong dispersive regime.

To that end, we first characterize our device by measuring the coherence properties of the qubit and the phonon mode, as well as the coupling strength between them. Using standard cQED techniques<sup>22,23</sup>, we find an energy relaxation time for the qubit of  $T_1 = 10.2 \pm 0.4 \mu\text{s}$ , a Ramsey decoherence time of  $T_{2e}^* = 10.5 \pm 0.5 \mu\text{s}$  and an echo decoherence time of  $T_2^* = 11.6 \pm 0.4 \mu\text{s}$ . Direct driving and readout of the qubit is performed at a detuning of  $\Delta_{\text{rest}}/2\pi = -4.1$  MHz from the LG-00 phonon mode of interest. Tuning the qubit into resonance with the phonon mode then allows the two systems to coherently exchange energy through the resonant JC interaction, which is used to implement qubit–phonon SWAP operations for characterizing the phonon mode and initializing it in a quantum state in subsequent experiments<sup>1,18</sup>. The phonon mode spectrum and coupling to the qubit are measured by exciting the qubit at  $\Delta_{\text{rest}}$  and then tuning it to different frequencies and reading out the qubit state after a variable time (Fig. 1c). We observe two oscillatory features centred around 5.9741 and 5.9752 GHz, corresponding to vacuum Rabi oscillations between the qubit and the LG-00 and LG-10 phonon modes, respectively. From these vacuum Rabi oscillations, we extract a coupling strength for the LG-00 mode of  $g/2\pi = 259.5 \pm 0.3$  kHz.

Using protocols described in previous work<sup>18</sup>, we find  $T_1 = 81.0 \pm 1.1 \mu\text{s}$  and  $T_2^* = 138.0 \pm 2.5 \mu\text{s}$  for the phonon mode (Fig. 1d), corresponding to a dephasing time of  $T_\phi = 932.0 \pm 112.0 \mu\text{s}$ . During the delay times for both measurements, we tune the qubit back to  $\Delta_{\text{rest}}$ . This allows us to measure the intrinsic phonon coherence without a substantial effect due to Purcell decay through the qubit. Note that both qubit and phonon coherence times have considerably increased from previous devices<sup>1</sup>.

The improved coherence of our system allows us to operate it in the strong dispersive regime, which we now demonstrate through phonon-number-resolving measurements of the qubit spectrum. We create coherent states in our phonon mode by driving it on resonance with a microwave pulse of length  $10 \mu\text{s}$  as the qubit is at  $\Delta_{\text{rest}}$ . After the phonon state preparation, we decrease the detuning to  $\Delta_{\text{coherent}}/2\pi = -1.2$  MHz to reach a regime where the dispersive shift of the qubit frequency due to a single phonon should be much larger than the qubit's intrinsic linewidth  $\gamma_2^*/2\pi = 15.1$  kHz. We then perform qubit spectroscopy using a probe pulse with a bandwidth of 10.6 kHz, less than  $\gamma_2^*$ , thus ensuring that the qubit linewidth is not substantially broadened. Finally, a standard dispersive measurement of the qubit population via the microwave cavity is performed with the qubit at frequency  $\Delta_{\text{rest}}$ . The resulting qubit spectra for different amplitudes of the displacement drive on the phonon modes is shown in Fig. 2a. At larger amplitudes, we observe multiple resonances, as expected from the dispersive interaction with a superposition of phonon Fock states. We fit each spectrum to a sum of Voigt profiles to extract the height of the peaks. These heights then give the population  $P_n$  of each Fock state  $|n\rangle$  after normalizing such that  $\sum_n P_n = 1$ . From fitting a Poisson distribution to the measured

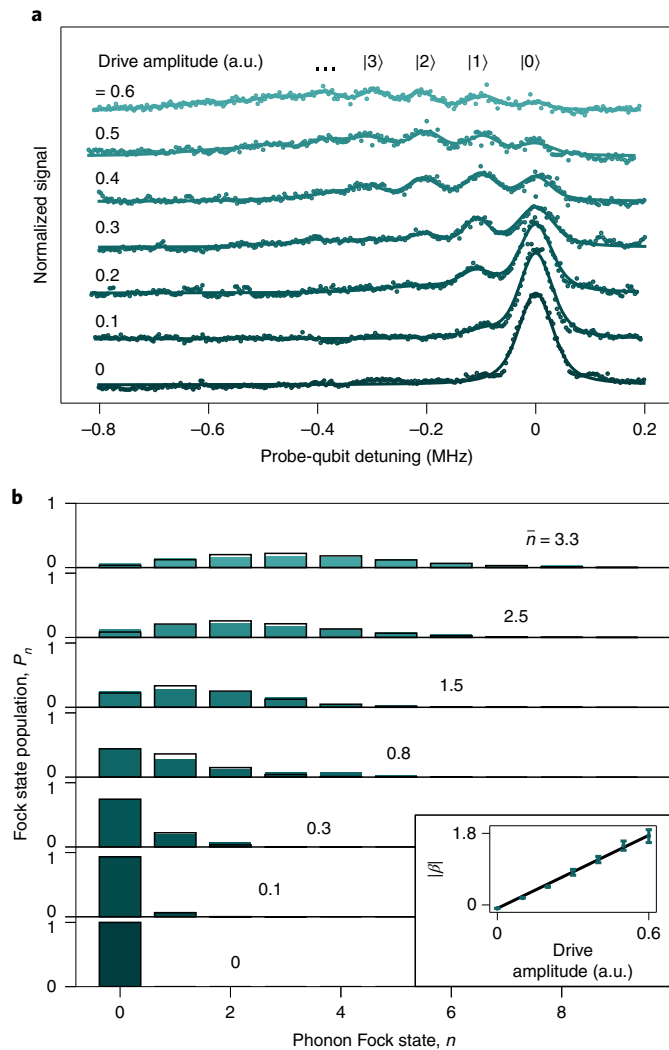


**Fig. 2 | Dispersive measurement of phonon coherent states.**

**a**, Spectroscopy of the qubit as it is dispersively coupled to coherent phonon states prepared using displacement drives with the indicated amplitudes. The solid lines are fits to the sums of Voigt profiles, used to extract the Fock state populations  $P_n$ . The data are rescaled so that the total population is normalized, and each trace is vertically shifted by 0.5 for clarity. The  $|0\rangle$  peak is aligned for all the spectra to correct for slow qubit frequency fluctuations. **b**,  $P_n$  extracted from the measurements in **a** and the corresponding mean phonon number  $\bar{n}$  from fit to the Poisson distribution. The black boxes are the ideal Poisson distributions assuming an average phonon number of  $\bar{n}$ . The inset shows the linear relation between the displacement drive amplitude and  $|\beta| = \sqrt{\bar{n}}$ . The error bars represent one standard deviation of the fit uncertainty of the Poisson distribution.

populations, we obtain the mean phonon number  $\bar{n}$  of the coherent state that most closely matches the data (Fig. 2b). We find a linear dependence of the extracted coherent state amplitude  $|\beta| = \sqrt{\bar{n}}$  on the drive amplitude (Fig. 2b, inset), indicating the capability of performing coherent displacements of the phonon mode up to  $|\beta| = 1.9$ . Additionally, these measurements provide a calibration between the drive amplitude we set and the resulting displacement amplitude (Supplementary Fig. 1). Both these results will be used in the experiments that follow.

We now extend our analysis further to non-classical states prepared in the phonon mode. We repeat the measurement procedure adopted for Fig. 2a, but now with the phonon mode initialized in

the Fock states containing  $M$  phonons. We perform this initialization up to  $M = 3$  using repeated qubit excitations and SWAP operations with the phonon mode<sup>1</sup>. In this case, we set the detuning during the dispersive interaction to be  $\Delta_{\text{Fock}}/2\pi = -0.8$  MHz. The smaller detuning leads to larger  $\chi$  and better resolved peaks in the qubit spectrum at the expense of a less ideal dispersive approximation. Figure 3a shows the qubit spectroscopy measurements, each resulting in one prominent peak corresponding to the target Fock state. Additionally, smaller peaks corresponding to a finite population in lower Fock states can be seen, as expected from imperfect SWAP operations and phonon decay during preparation and measurement. Calculating the difference in frequency between the  $|0\rangle$  peak for the  $M = 0$  case and the  $|1\rangle$  peak for the  $M = 1$  case yields  $\chi_{\text{Fock}}/2\pi = -147$  kHz. We observe slightly smaller frequency differences between the peaks corresponding to higher phonon populations (explained in Supplementary Section D and Supplementary Fig. 2). The measured frequency differences are compatible with the dispersive shifts we expect from simulations. Again, we confirm the operation of our system in the strong dispersive regime.

The change in qubit frequency due to different phonon states can also be observed in the time domain by performing Ramsey-type measurements on the qubit<sup>11,24</sup>. After initializing the phonon mode in a Fock state as above, we prepare the qubit in the superposition state  $(|g\rangle + |e\rangle)/\sqrt{2}$ . We then move the qubit frequency from  $\Delta_{\text{rest}}$  to  $\Delta_{\text{Ramsey}}/2\pi = -1.9$  MHz from the phonon mode, where we let it dispersively interact with the phonon state for a variable time  $t$ . Here  $\Delta_{\text{Ramsey}}$  is chosen to be larger than  $\Delta_{\text{Fock}}$  to minimize deviations from the ideal dispersive Hamiltonian while still maintaining a large enough  $\chi$ . Finally, we move the qubit back to  $\Delta_{\text{rest}}$ , perform the second  $\pi/2$  pulse and read out the qubit state. The phase of the second  $\pi/2$  pulse is calibrated such that there is no oscillation in the Ramsey measurement corresponding to the phonon  $|0\rangle$  state. The measured data are shown in Fig. 3b. We observe decaying oscillations at frequencies approximately equal to the dispersive shift  $M|\chi_{\text{Ramsey}}|/2\pi = M \times 70$  kHz. To explain this observation, we note that in the frame rotating at the bare qubit frequency  $\omega_q$ , the initial superposition state evolves due to the dispersive interaction term into  $(|g\rangle + \exp(-iM\chi_{\text{Ramsey}}t)|e\rangle)/\sqrt{2}$ . After the second  $\pi/2$  pulse of the Ramsey sequence, this relative phase is mapped onto the qubit population. The striking feature of this protocol is that for an interaction time  $t_0 = \pi/|\chi_{\text{Ramsey}}|$ , the measurement result in the ideal case is  $|\sigma_z\rangle = \cos(M\pi)$ , which yields the phonon number parity  $\Pi$ . In Fig. 3b, we can indeed observe that at time  $t_0 = 7.1$   $\mu$ s, an even (odd) Fock state results in a high (low) qubit population. We emphasize here that determining the parity with this procedure requires only a single measurement with interaction time  $t_0$  and does not reveal the underlying phonon distribution. It is, therefore, more efficient and more useful for bosonic error correction protocols than the alternative method of computing the parity using the  $P_n$  value extracted from the full qubit spectra as  $\Pi = \sum_n (-1)^n P_n$ . We compare the two methods in Fig. 3c. As expected, the prepared even (odd) Fock states show positive (negative) parity for both spectroscopy and Ramsey-type measurements. For higher phonon Fock states, both methods show parities close to zero, which we attribute to imperfect state preparation and decoherence, as explained earlier. We also note here that the residual JC interaction due to a finite  $g/|\Delta_{\text{Ramsey}}| \approx 0.14$  results in a finite probability for energy exchange between the phonon mode and qubit that scales as  $g^2/\Delta_{\text{Ramsey}}^2$ , which limits the QND nature of our current measurements. Improving this figure of merit will be the subject of our future work. This can be achieved by increasing  $g$  and the qubit and phonon coherences, which would allow for a smaller  $g/\Delta$  and maintaining a high dispersive cooperativity  $C \equiv 4\chi^2 T_2^* T_2^*$ , which is currently  $C_{\text{Ramsey}} = 594$ . Note our definition of  $C$  takes into account the fact that the qubit and phonon  $T_2^*$  values, rather than  $T_1$  values, are the relevant values that determine the quality of protocols that we demonstrate in this work.



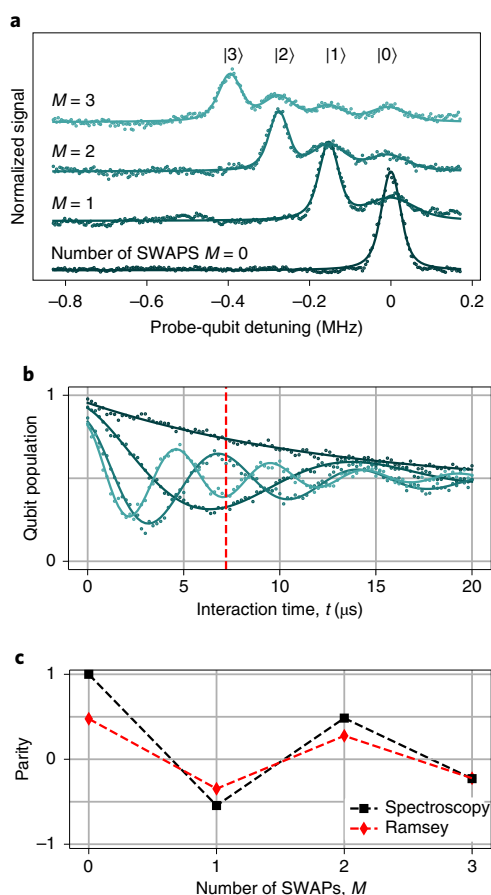


**Fig. 3 | Dispersive measurement of phonon Fock states. a,b**, Spectroscopy (a) and Ramsey (b) measurements of the qubit when it is dispersively coupled to the phonon mode, following state preparation that ideally results in Fock states containing  $M$  phonons. For **a**, the same procedure as in Fig. 2a was used for fitting and rescaling the data to extract the phonon populations. In **b**, the solid lines are fits with an exponentially decaying cosine. Oscillations do not start from unity due to a finite qubit population after the phonon state preparation. The dashed red line indicates the Ramsey interrogation time used for measuring the parity of the prepared state. **c**, Parity of the prepared phonon Fock states measured by spectroscopy (black) and Ramsey (red) measurements. The dashed lines are guides to the eye. The error bars are smaller than the markers.

The measurement of the phonon state parity together with coherent displacements gives us the necessary tools to perform Wigner tomography. This is enabled by the fact that the Wigner function can be expressed as displaced parity measurements<sup>25</sup>. We again emphasize that in contrast to previous work (where the parity was determined by first extracting the phonon number distribution from time-resolved measurements of the resonant qubit–phonon interaction<sup>1</sup>), here we are able to measure the parity at each position in the phase space with a single averaged measurement on the qubit. Figure 4a shows the sequence used to perform Wigner tomography of the phonon mode in the  $|1\rangle$  state (for other states, the sequence differs only in the state preparation step at the beginning). This is followed by a coherent displacement of the phonon state by complex amplitude  $\beta$ . Our device suffers from slow qubit frequency fluctuations on the  $\sim 10$  kHz frequency scale common in superconducting qubits<sup>26</sup>. In contrast to most cQED systems, however, this is comparable to our dispersive shift. Therefore, we improve our parity measurement protocol by introducing a dynamical decoupling pulse sequence to mitigate the effect of low-frequency noise as follows: we

initialize the qubit in the state  $(|g\rangle + |e\rangle)/\sqrt{2}$  and then tune its frequency to  $\Delta_{\text{Ramsey}}$ . After an interaction time of  $\pi/(2|\chi_{\text{Ramsey}}|) = 3.53 \mu\text{s}$ , the qubit superposition acquires a relative phase of  $n\pi/2$ . We then move the qubit frequency back to its rest point, apply a  $\pi$  pulse and move the qubit frequency to a detuning of  $-\Delta_{\text{Ramsey}}$ , flipping the sign of the dispersive shift. In combination with the echo pulse, this results in a total relative phase accumulation of  $n\pi$  after another interaction time  $\pi/(2|\chi_{\text{Ramsey}}|)$ . The relative phase that changes due to low-frequency noise (such as shot-to-shot qubit frequency jumps) does not depend on the sign of the detuning and is thus cancelled out. The echo sequence ends by taking the qubit frequency back to  $\Delta_{\text{rest}}$  and applying a second  $\pi/2$  pulse, whose phase is calibrated to compensate the effect caused by the Stark-shift drive used to change the qubit frequency. We also take additional measures to mitigate the effects of the residual JC interaction due to finite  $g/\Delta$  on our Wigner tomography. The first-order effect is a  $\beta$ -dependent deviation from an ideal parity measurement and is cancelled by averaging the data taken with four different qubit-drive phases, indicated by  $\theta$  in Fig. 4a. The remaining effect is an interaction-time-dependent constant offset of the Wigner function that oscillates with a frequency much faster than  $|\chi|$ . This allows us to precisely choose the interaction time to minimize this effect. More details on both these effects are given in Supplementary Section E and Supplementary Figs. 3 and 4.

Figure 4b shows the measured Wigner functions for the phonon mode prepared in the states  $|0\rangle$ ,  $(|0\rangle + |1\rangle)/\sqrt{2}$ ,  $|1\rangle$  and  $|2\rangle$  (Supplementary Fig. 5). For comparison, Fig. 4c shows the Wigner functions obtained from a master equation simulation<sup>27</sup> of our experimental sequence consisting of state preparation, displacement and dispersive interaction, using the full JC Hamiltonian, including finite pulse lengths and both decay and decoherence in the system. The results are in good agreement with the measurements and reproduce features that would not be present in the ideal case. For example, note that the Wigner function for  $|2\rangle$  does not show circular symmetry due to imperfect state preparation, and the non-zero values of the Wigner function at large displacements can again be attributed to the residual JC interaction. Supplementary Fig. 6 shows the reconstructions of the physical state corresponding to the measured Wigner functions. The discrepancy in both measurements and simulations from the ideal Wigner functions, however, is mainly due to qubit and both phonon decay and decoherence.

Our results show that the dispersive measurements of mechanical quantum states are now possible in  $\hbar$ BAR-type cQAD systems. We achieved this through improvements to the coherence properties of both qubit and phonon mode to reach the strong dispersive regime. We carefully chose the qubit–phonon detuning to reach a compromise between ensuring that the dispersive interaction is strong enough to allow for coherent operations and remaining in the dispersive regime. For the purpose of performing quantum state tomography, we devised protocols that mitigated to first order the effect of qubit–phonon energy exchange due to the residual JC interaction and qubit frequency fluctuations that are non-negligible compared with  $\chi$ . However, the decoherence and energy exchange during the measurement still degrade the quality of single-shot QND measurements that are needed in, for example, error correction protocols. Therefore, continued improvements to the basic device properties of  $\hbar$ BAR devices remain crucial, and further exploration of the large space of design parameters and their effect on device performance is the subject of our ongoing work (Supplementary Table 1).

Although quantum operations that make use of the dispersive interaction are useful ingredients for quantum information processing, they can also be seen as the first step towards a much broader range of future experiments and applications, such as storage, processing or transduction of quantum information<sup>9,17,28,29</sup>. Some

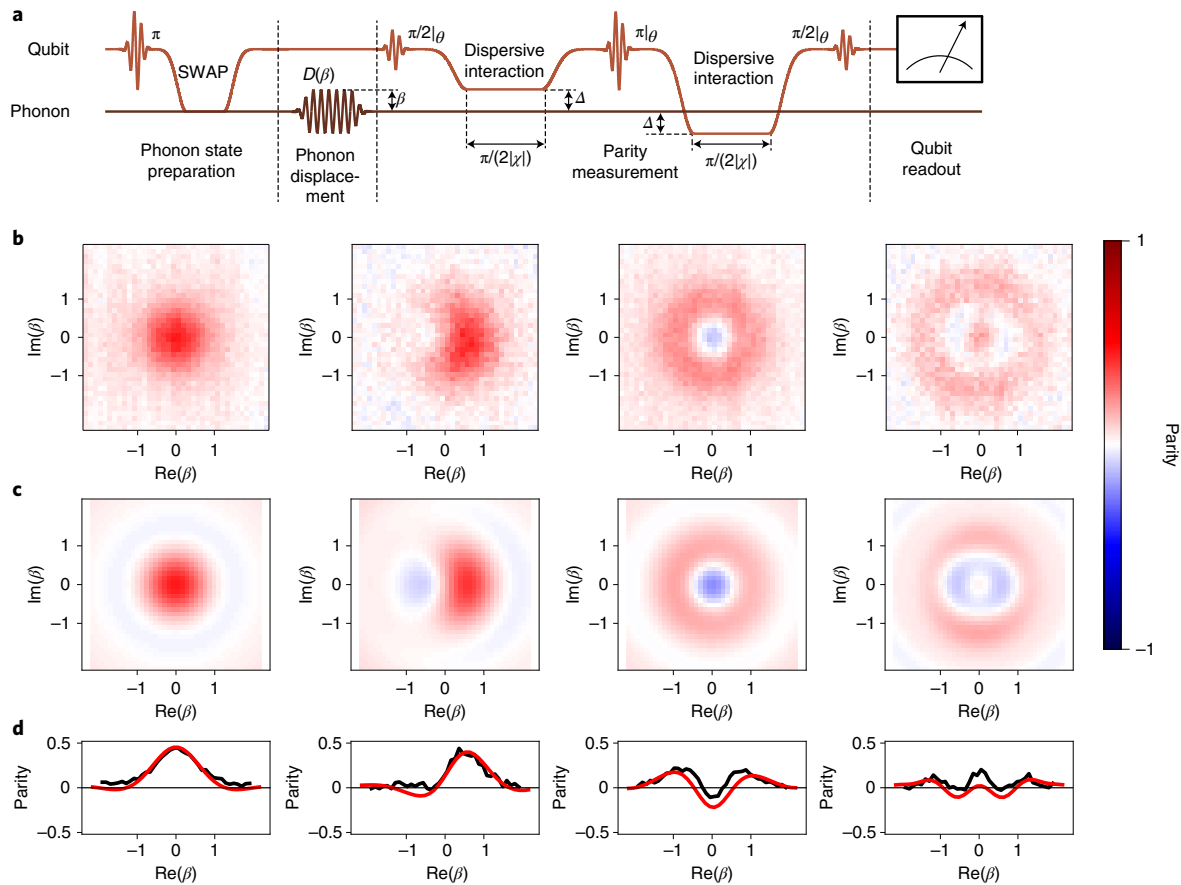


**Fig. 4 | Wigner tomography of non-classical phonon states.** **a**, Sequence used for the Wigner tomography of a phonon mode prepared in  $|1\rangle$  (details in the main text). **b**, Measured Wigner functions of the phonon mode prepared in (from left to right)  $|0\rangle$ ,  $\frac{1}{\sqrt{2}}(|0\rangle + |1\rangle)$ ,  $|1\rangle$  and  $|2\rangle$ . The axes are calibrated using the data in Fig. 2 (Supplementary Fig. 1). **c**, Wigner functions obtained from the master equation simulations of the JC Hamiltonian. The axes are calibrated by fitting the simulated density matrix of the phonon mode after a displacement. **d**, Cuts along the  $\text{Im}(\beta) = 0$  axis for the measured results shown in **b** (black) and simulation results shown in **c** (red).

applications are unique to mechanical systems. For example, the quantum states of mechanical resonators such as Fock state superpositions and Schrödinger cat states have been proposed as resources for quantum-enhanced frequency or force sensing<sup>30</sup> and testing modifications to quantum mechanics at macroscopic scales<sup>9,31</sup>. Many existing protocols for preparing such complex quantum states make direct use of the dispersive interaction<sup>32,33</sup>. At the same time, other protocols for the quantum control of bosonic modes, such as parametrically driven multimode gates<sup>29,34</sup> or autonomous stabilization of non-trivial quantum states<sup>35</sup>, do not directly make use of the dispersive Hamiltonian. However, the requirements on coupling strengths and coherences to perform these operations are effectively similar to the strong dispersive regime. Our results suggest that these demonstrations will soon be within reach for cQAD devices.

### Online content

Any methods, additional references, Nature Research reporting summaries, source data, extended data, supplementary information, acknowledgements, peer review information; details of author contributions and competing interests; and statements of data and code availability are available at <https://doi.org/10.1038/s41567-022-01591-2>.

Received: 22 January 2022; Accepted: 21 March 2022;  
Published online: 12 May 2022

### References

1. Chu, Y. et al. Creation and control of multi-phonon Fock states in a bulk acoustic-wave resonator. *Nature* **563**, 666–670 (2018).
2. Bienfait, A. et al. Quantum erasure using entangled surface acoustic phonons. *Phys. Rev. X* **10**, 021055 (2020).
3. Arrangoiz-Arriola, P. et al. Resolving the energy levels of a nanomechanical oscillator. *Nature* **571**, 537–540 (2019).
4. Sletten, L. R., Moores, B. A., Viennot, J. J. & Lehnert, K. W. Resolving phonon Fock states in a multimode cavity with a double-slit qubit. *Phys. Rev. X* **9**, 021056 (2019).
5. Kotler, S. et al. Direct observation of deterministic macroscopic entanglement. *Science* **372**, 622–625 (2021).
6. Ockeloen-Korppi, C. F. et al. Stabilized entanglement of massive mechanical oscillators. *Nature* **556**, 478–482 (2018).
7. MacCabe, G. S. et al. Nano-acoustic resonator with ultralong phonon lifetime. *Science* **370**, 840–843 (2020).
8. Tsaturyan, Y., Barg, A., Polzik, E. S. & Schliesser, A. Ultracoherent nanomechanical resonators via soft clamping and dissipation dilution. *Nat. Nanotechnol.* **12**, 776–783 (2017).
9. Chamberland, C. et al. Building a fault-tolerant quantum computer using concatenated cat codes. *PRX Quantum* **3**, 010329 (2022).
10. Pikovski, I., Vanner, M. R., Aspelmeyer, M., Kim, M. S. & Brukner, Č. Probing Planck-scale physics with quantum optics. *Nat. Phys.* **8**, 393–397 (2012).
11. Bertet, P. et al. Direct measurement of the Wigner function of a one-phonon Fock state in a cavity. *Phys. Rev. Lett.* **89**, 200402 (2002).
12. Schuster, D. I. et al. Resolving photon number states in a superconducting circuit. *Nature* **445**, 515–518 (2007).
13. Walter, T. et al. Rapid high-fidelity single-shot dispersive readout of superconducting qubits. *Phys. Rev. Appl.* **7**, 054020 (2017).
14. Rosenblum, S. et al. Fault-tolerant detection of a quantum error. *Science* **361**, 266–270 (2018).

15. Ofek, N. et al. Extending the lifetime of a quantum bit with error correction in superconducting circuits. *Nature* **536**, 441–445 (2016).
16. Hu, L. et al. Quantum error correction and universal gate set operation on a binomial bosonic logical qubit. *Nat. Phys.* **15**, 503–508 (2019).
17. Chu, Y. & Gröblacher, S. A perspective on hybrid quantum opto- and electromechanical systems. *Appl. Phys. Lett.* **117**, 150503 (2020).
18. Chu, Y. et al. Quantum acoustics with superconducting qubits. *Science* **358**, 199–202 (2017).
19. Satzinger, K. J. et al. Simple non-galvanic flip-chip integration method for hybrid quantum systems. *Appl. Phys. Lett.* **114**, 173501 (2019).
20. Blais, A., Huang, R.-S., Wallraff, A., Girvin, S. M. & Schoelkopf, R. J. Cavity quantum electrodynamics for superconducting electrical circuits: an architecture for quantum computation. *Phys. Rev. A* **69**, 062320 (2004).
21. Koch, J. et al. Charge-insensitive qubit design derived from the Cooper pair box. *Phys. Rev. A* **76**, 042319 (2007).
22. Krantz, P. et al. A quantum engineer's guide to superconducting qubits. *Appl. Phys. Rev.* **6**, 021318 (2019).
23. Blais, A., Grimsmo, A. L., Girvin, S. M. & Wallraff, A. Circuit quantum electrodynamics. *Rev. Mod. Phys.* **93**, 025005 (2021).
24. Sun, L. et al. Tracking photon jumps with repeated quantum non-demolition parity measurements. *Nature* **511**, 444–448 (2014).
25. Royer, A. Wigner function as the expectation value of a parity operator. *Phys. Rev. A* **15**, 449–450 (1977).
26. Burnett, J. J. et al. Decoherence benchmarking of superconducting qubits. *npj Quantum Inf.* **5**, 54 (2019).
27. Johansson, J. R., Nation, P. D. & Nori, F. QuTiP: an open-source Python framework for the dynamics of open quantum systems. *Comput. Phys. Commun.* **183**, 1760–1772 (2012).
28. Pechal, M., Arrangoiz-Arriola, P. & Safavi-Naeini, A. H. Superconducting circuit quantum computing with nanomechanical resonators as storage. *Quantum Sci. Technol.* **4**, 015006 (2019).
29. Hann, C. T. et al. Hardware-efficient quantum random access memory with hybrid quantum acoustic systems. *Phys. Rev. Lett.* **123**, 250501 (2019).
30. McCormick, K. C. et al. Quantum-enhanced sensing of a single-ion mechanical oscillator. *Nature* **572**, 86–90 (2019).
31. Penrose, R. On gravity's role in quantum state reduction. *Gen. Relat. Gravit.* **28**, 581–600 (1996).
32. Vlastakis, B. et al. Deterministically encoding quantum information using 100-photon Schrödinger cat states. *Science* **342**, 607–610 (2013).
33. Heeres, R. W. et al. Implementing a universal gate set on a logical qubit encoded in an oscillator. *Nat. Commun.* **8**, 94 (2017).
34. Gao, Y. Y. et al. Entanglement of bosonic modes through an engineered exchange interaction. *Nature* **566**, 509–512 (2019).
35. Leghtas, Z. et al. Confining the state of light to a quantum manifold by engineered two-photon loss. *Science* **347**, 853–857 (2015).

**Publisher's note** Springer Nature remains neutral with regard to jurisdictional claims in published maps and institutional affiliations.

© The Author(s), under exclusive licence to Springer Nature Limited 2022

**Data availability**

Source data are provided with this paper. All other data that support the plots within this paper and other findings of this study are available from the corresponding authors upon reasonable request.

**Code availability**

Analysis and simulation codes that support the findings of this study are available from the corresponding authors upon reasonable request.

**Acknowledgements**

We thank X. Cao and A. deMello for help with the flip-chip-bonding process and J.-C. Besse for help with the qubit fabrication. We thank B. Li for providing support with the QuTiP simulations. The fabrication of devices was performed at the FIRST cleanroom of ETH Zürich and the BRNC cleanroom of IBM Zürich. M.F. acknowledge The Branco Weiss Fellowship—Society in Science, administered by the ETH Zürich.

**Author contributions**

U.v.L. and L.M. designed and fabricated the device. U.v.L. and M.B. constructed the parametric amplifier used for the qubit readout. M.B. wrote the experiment control

software. Y.Y., U.v.L. and M.B. performed the experiment and analysed the data. Y.Y. performed the QuTiP simulations of the experiment. M.F., M.B. and Y.C. performed the theoretical calculations. Y.C. supervised the work. U.v.L., Y.Y., M.B., M.F. and Y.C. wrote the manuscript.

**Competing interests**

The authors declare no competing interests.

**Additional information**

**Supplementary information** The online version contains supplementary material available at <https://doi.org/10.1038/s41567-022-01591-2>.

**Correspondence and requests for materials** should be addressed to Uwe von Lüpke or Yiwen Chu.

**Peer review information** *Nature Physics* thanks the anonymous reviewers for their contribution to the peer review of this work.

**Reprints and permissions information** is available at [www.nature.com/reprints](http://www.nature.com/reprints).